catalysts

MDPI

Article

Promoting Effect of the Core-Shell Structure of MnO_2@TiO_2 Nanorods on SO_2 Resistance in Hg^0 Removal Process

Xiaopeng Zhang, Xiangkai Han, Chengfeng Li, Xinxin Song, Hongda Zhu, Junjiang Bao, Ning Zhang and Gaohong He *

State Key Laboratory of Fine Chemicals, School of Chemical Engineering at Panjin, Dalian University of Technology, Panjin 124221, China; xiaopengzhang@dlut.edu.cn (X.Z.); hanxiangkai@mail.dlut.edu.cn (X.H.); li_cf@mail.dlut.edu.cn (C.L.); songxinxinhuagong@163.com (X.S.); dada@mail.dlut.edu.cn (H.Z.); baojj@dlut.edu.cn (J.B.); zhangning@dlut.edu.cn (N.Z.)

* Correspondence: hgaohong@dlut.edu.cn; Tel.: +86-427-2631916

Received: 5 December 2019; Accepted: 2 January 2020; Published: 3 January 2020

Abstract: Sorbent of αMnO_2 nanorods coating TiO_2 shell (denoted as αMnO_2-NR@TiO_2) was prepared to investigate the elemental mercury (Hg^0) removal performance in the presence of SO_2. Due the core-shell structure, αMnO_2-NR@TiO_2 has a better SO_2 resistance when compared to αMnO_2 nanorods (denoted as αMnO_2-NR). Kinetic studies have shown that both the sorption rates of αMnO_2-NR and αMnO_2-NR@TiO_2, which can be described by pseudo second-order models and SO_2 treatment, did not change the kinetic models for both the two catalysts. In contrast, X-ray photoelectron spectroscopy (XPS) results showed that, after reaction in the presence of SO_2, S concentration on αMnO_2-NR@TiO_2 surface is lower than on αMnO_2-NR surface, which demonstrated that TiO_2 shell could effectively inhibit the SO_2 diffusion onto MnO_2 surface. Thermogravimetry-differential thermosgravimetry (TG-DTG) results further pointed that SO_2 mainly react with TiO_2 forming $Ti(SO_4)O$ in αMnO_2-NR@TiO_2, which will protect Mn from being deactivated by SO_2. These results were the reason for the better SO_2 resistance of αMnO_2-NR@TiO_2.

Keywords: core-shell structure; αMnO_2 nanorods; elemental mercury removal; SO_2 resistance

1. Introduction

The emission of mercury from coal-fired power plants has drawn wide public concern in modern society. Mercury emissions are a long-term threat to human health and the environment because of extreme toxicity, persistence, and bioaccumulation. Therefore, controlling mercury emitted from coal-fired power plants has practical significance. Mercury in coal combustion flue gas is mainly present in three forms: Elemental mercury (Hg^0), oxidized mercury (Hg^{2+}), and particulate-bound mercury (Hg^p). Particulate-bound mercury (Hg^p) can be removed by electrostatic precipitators (ESP) and fabric filters (FF), while oxidized mercury (Hg^{2+}) can be captured by wet flue gas desulfurization system (WFGD). However, existing air pollution control devices can hardly remove Hg^0 due to its high volatility and low solubility.

Hg^0 capture with specific adsorbents is a usual way to control Hg^0 emissions from coal-fired power plants [1]. Activated cabon (AC) has been widely used for the adsorption of Hg^0 in coal-fired flue gas [2,3]. However, a huge amount of AC needs to be injected into flue gas because of its low Hg^0 capture capacity, which leads to a high operating cost of this technology. Sulfur or halogen modification can enhance adsorption ability of AC [4,5]. However, the injected AC is usually captured together with fly ash by particulate control device, and the Hg^0 adsorbed on AC will influence the

fly ash utilization [6]. Therefore, alternative economic sorbents with high Hg^0 removal efficiency are necessary.

Oxides, such as CuO_x [7,8], FeO_x [9,10], CeO_x [11,12] and MnO_x [13–15], with high redox properties, exhibit great potential for Hg^0 adsorption. Among these oxides, MnO_x is a commonly available and inexpensive material has received extensive attention due to the redox couples of Mn^{2+}/Mn^{3+} and Mn^{3+}/Mn^{4+} [16]. Electronic shift between the different valence states of Mn is active and leads to a high redox capacity. Stefano Cimino et al. [14] investigated the Hg^0 removal performance of Mn/TiO_2 and found that Hg^0 capture efficiency was about 57% at 70 °C. After modification by some other transition metal oxides, Mn-based materials, such as Mn-FeO_x [15], Mn-ZrO_x [17], Mn-CeO_x [18], and Mn-CuO_x [19] can remove Hg^0 better. Furthermore, it has been reported that the shape and crystallographic phases of Mn based sorbents have serious effects on Hg^0 removal performance. Xu et al. [20] synthesized three different crystallographic phases of MnO_2 and found that α-MnO_2 had the highest capacity due to its larger surface area and oxidizability. Chalkidis et al. [21] pointed out that MnO_2 nano-rods possessed good Hg^0 removal capacity owing to the higher surface adsorbed oxygen species.

However, Mn-based sorbents usually have a poor SO_2 resistance as SO_2 can easily react with Mn, thereby forming $MnSO_4$ and leading to a largely suppressed Hg^0 removal activity. Even a little amount of SO_2 will results in serious inhibited effects on Hg^0 removal process. Our previous work has indicated that Ce-Zr modified Mn sorbent will be totally deactivated in 1h after the introduction of 50 ppm SO_2 due to SO_2 poisoning Mn forming $MnSO_4$ [22]. TiO_2 is a traditional way to enhance the SO_2 resistance of MnO_x [23] as TiO_2 can inhibit the deposition of sulfates on sorbents surface [24]. But the Hg^0 removal activity of MnO_x/TiO_2 is unsatisfactory because the active component of Mn is still exposed in SO_2 atmosphere. Core-shell is a structure with active component core and supporting components shell. The shell can inhibit the interaction between SO_2 and sorbent surface and efficiently protect active component core [25]. Therefore, synthesizing a core-shell structure with MnO_x core and TiO_2 shell may obtain a better SO_2 resistance.

Inspired by this, αMnO_2 nanorods and αMnO_2 nanorods coating TiO_2 shell were synthesized in the present work to investigate the Hg^0 removal efficiency in the presence of SO_2. Thermo-gravimetric (TG) and X-ray photoelectron spectroscopy (XPS) were performed to determine the role of SO_2 in the Hg^0 oxidation and adsorption processes and a probable mechanism of SO_2 influence was deduced based on XPS and TG results. The kinetic model of the Hg^0 adsorption process was examined as well.

2. Results and Discussion

2.1. Structure Characterization

Scanning electron microscopy (SEM) and transmission electron microscopy (TEM) were performed to investigate the morphologic and structural properties of αMnO_2-NR and αMnO_2-NR@TiO_2. Figure 1a,a′ show SEM and TEM images of αMnO_2-NR. It can be seen that αMnO_2-NR has a uniform nanorod structure with an average diameter of about 100 nm. As shown in Figure 1b, for αMnO_2-NR@TiO_2, the uniform nanorod structure is well-retained after being coated with TiO_2 and the packing state of this sample is similar to αMnO_2-NR. The surface of αMnO_2-NR@TiO_2 are rougher when compared to αMnO_2-NR, and the average diameter increases to 150 nm due to the TiO_2 coating. The average length of the αMnO_2-NR@TiO_2 is about 2–3 μm (shown in Figure 1c). As shown in Figure 1b′, an obvious dividing line can be detected between MnO_2 core and TiO_2 shell, and the shell with thickness of about 30 nm is well dispersed outside of the αMnO_2-NR.

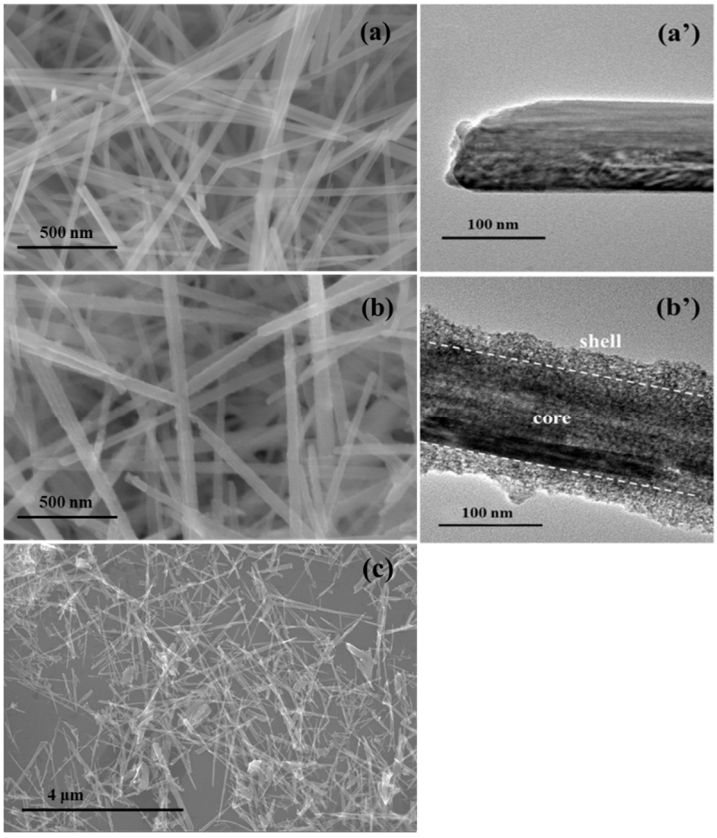

Figure 1. Scanning electron microscopy (SEM), and transmission electron microscopy (TEM) images of (**a**,**a'**) αMnO_2-NR; (**b**,**b'**), and (**c**) αMnO_2-NR@TiO_2.

N_2 sorption-desorption isotherms of the samples are shown in Figure 2. Both αMnO_2-NR and αMnO_2-NR@TiO_2 exhibit a type IV adsorption isotherm, according to the definition of IUPAC, which means that αMnO_2-NR and αMnO_2-NR@TiO_2 have a mesoporous structure. The surface areas, pore volumes, and average pore diameters of the sorbents are illustrated in Table 1. BET surface areas of the two sorbents are similar, suggesting that TiO_2 coating does not change the structure of αMnO_2-NR a lot. This result consists with SEM results.

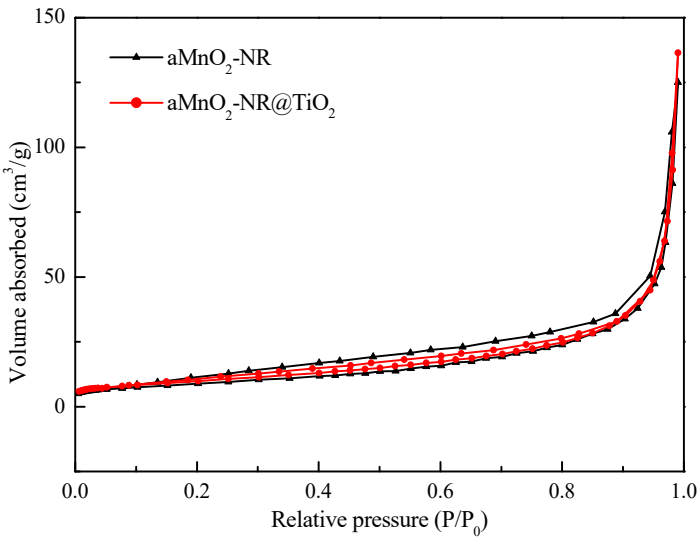

Figure 2. N_2 sorption-desorption isotherms for the sorbents.

Table 1. Pore structure analysis of the sorbents.

Samples	BET Surface Area (m^2/g)	Pore Volume (cm^3/g)	Average Pore Diameter (nm)
αMnO_2-NR	29.103	0.192	5.428
αMnO_2-NR@TiO_2	32.985	0.207	4.186

X-ray diffractometer (XRD) patterns of the two catalysts are shown in Figure 3. All the peaks in XRD pattern of αMnO_2-NR and αMnO_2-NR@TiO_2 were indexed to cryptomelane type α-MnO_2 (JCPDS 44-0141, tetragonal, *I*4/m, a = b = 0.978 nm, c = 0.286 nm). The intensity of diffraction peaks for the two samples is almost the same. It means that TiO_2 shell does not influence the dispersion of αMnO_2-NR, which is great agreement with BET and SEM results.

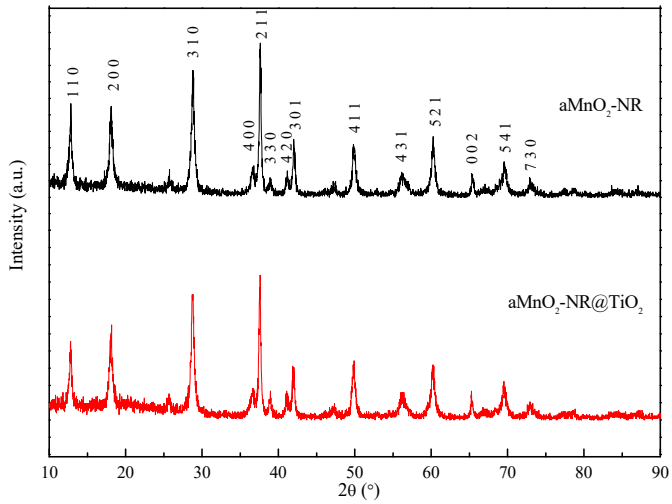

Figure 3. X-ray diffractometer (XRD) patterns of αMnO_2-NR and αMnO_2-NR@TiO_2.

2.2. Hg^0 Adsorption

2.2.1. Hg^0 Adsorption Performance

Breakthrough experiments were performed to investigate the Hg^0 adsorption performance of the two sorbents. A blank test was also performed and the results is shown in Figure S1. It can be seen that the outlet Hg^0 concentration is stable when no sorbent was loaded in the fixed-bed reactor. As shown in Figure 4, the Hg^0 removal efficiency of αMnO_2-NR is about 92% at the beginning of the test and it decreases to 41% after 130 min reaction. When it comes to αMnO_2-NR@TiO_2, the Hg^0 removal efficiency at the beginning of the test is about 81% which is lower than that of αMnO_2-NR. But it is about 43% at the end of the test suggesting a more stable removal activity. These results indicate that TiO_2 shell does not inhibit the Hg^0 diffusion from gas phase to the surface of αMnO_2-NR.

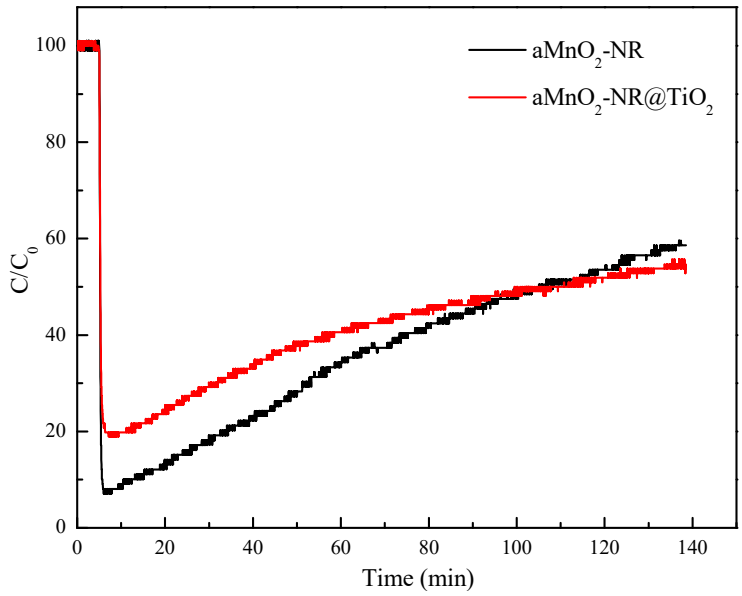

Figure 4. Hg^0 breakthrough curves of αMnO_2-NR and αMnO_2-NR@TiO_2 under pure N_2 atmosphere. Reaction condition: 150 °C, GHSV = 180,000 h^{-1}.

Figure 5 shows the effects of SO_2 on Hg^0 adsorption performance. For αMnO_2-NR, Hg^0 removal efficiency sharply declines from 55% to 14% during the 35 min reaction, when SO_2 is injected into flue gas. However, for αMnO_2-NR@TiO_2, the downward trend of Hg^0 removal efficiency is much slower and decreases from 76% to 43% in a 30 min test, and still has a Hg^0 removal efficiency of 25% after 80 min. These results confirm that TiO_2 shell can inhibit the direct interaction between SO_2 and MnO_2 surface, which will efficiently protect MnO_2 core from SO_2 poisoning.

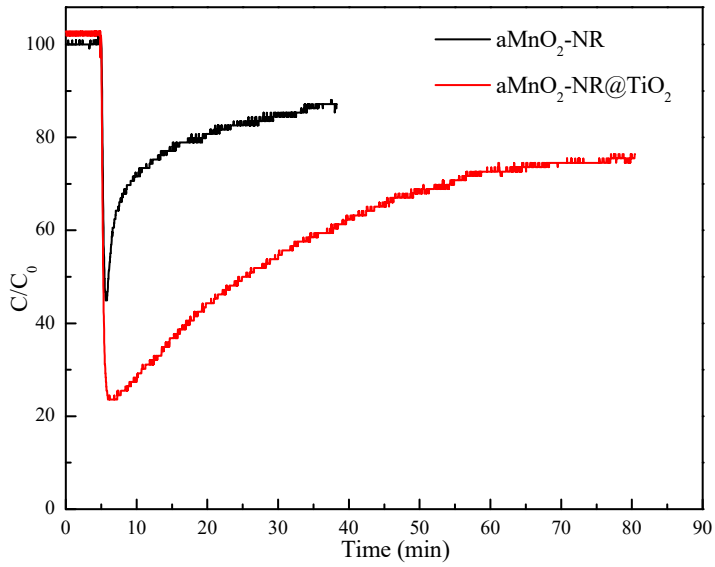

Figure 5. Hg^0 breakthrough curves of αMnO_2-NR and αMnO_2-NR@TiO_2 under 100 ppm SO_2, N_2 balanced. Reaction condition: 150 °C, GHSV = 180,000 h^{-1}.

αMnO_2-NR@TiO_2 was used to investigate reusability for Hg^0 removal. The results are shown in Figure 6. After 10 h Hg^0 adsorption test, αMnO_2-NR@TiO_2 reaches a Hg^0 adsorption equilibrium. And then, the sorbent was heated at 450 °C for 2 h to release the HgO on sorbent surface. It can be found that, after heated treatment, the Hg^0 adsorption efficiency and capacity of αMnO_2-NR@TiO_2 recovers to its original level. After two recycling, it still shows a good Hg^0 adsorption efficiency. Furthermore,

SEM results of the fresh and used αMnO_2-NR@TiO_2 (shown in Figure S2) show that recycle have no effect on the microstructure. These results suggest an outstanding reusability of αMnO_2-NR@TiO_2. The Hg^0 adsorption capacity of αMnO_2-NR@TiO_2 is 0.11 mg/g, it is good enough compared to other sorbents (shown in Table S1). The surface areas of the sorbents in the present work are relatively low thereby lowering the available surface active sites. αMnO_2-NR@TiO_2 with higher surface area will be studied in our following works, and may give a better Hg^0 adsorption capacity.

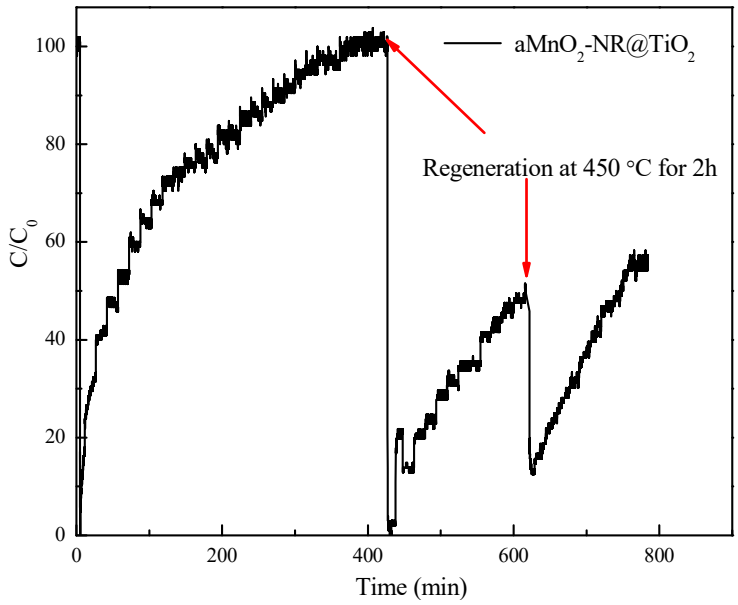

Figure 6. Hg^0 breakthrough curves of αMnO_2-NR@TiO_2 under pure N_2 atmosphere. Reaction condition: 150 °C, GHSV = 180,000 h^{-1}.

Hg^0 adsorption test of αMnO_2-NR@TiO_2 at different Hg^0 concentration was also investigated and the results are shown in Figure S3. With a doubled Hg^0 concentration, the breakthrough curve gets steep suggesting that αMnO_2-NR@TiO_2 will easily reach Hg^0 adsorption equilibrium at a higher Hg^0 concentration.

2.2.2. Structure-Activity Relationship

Fourier Transform Infrared Spectrometer (FTIR) was used to confirm the kind of surface active site for Hg^0 adsorption. As can be seen in Figure 7, the peaks at 429, 503, and 700 cm^{-1} correspond to Mn-O vibration [26], which becomes much weaker after reaction. It suggests that Mn-O group participates in Hg^0 adsorption process. According to previous work, the surface active oxygen species in Mn-O group should be the active sites for Hg^0 adsorption.

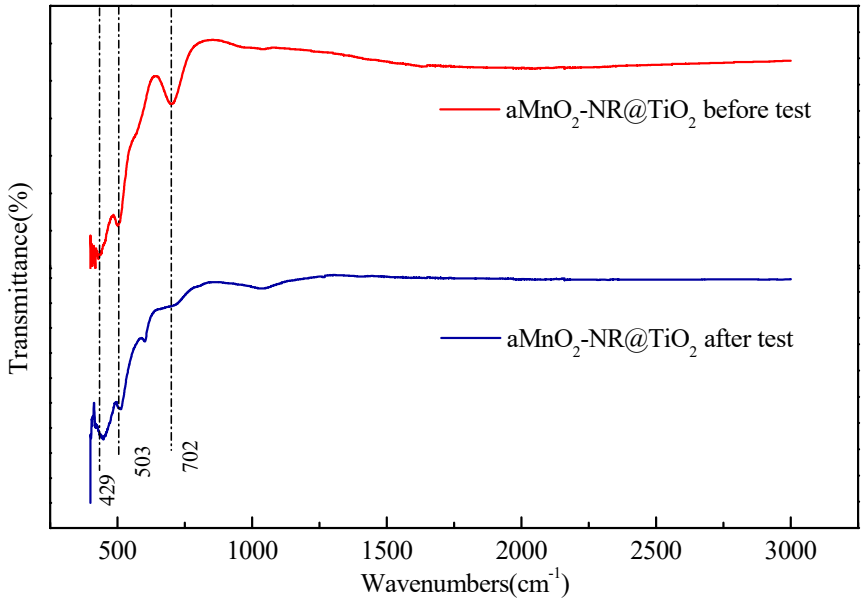

Figure 7. FTIR spectrum of αMnO_2-NR@TiO_2 before and after test.

2.3. Models of Adsorption Kinetics

In order to better illustrate the Hg^0 adsorption mechanisms of αMnO_2-NR and αMnO_2-NR@TiO_2, two popular models of pseudo-first order and pseudo-second order kinetic models, which have been widely used to investigate the adsorption process [27], were employed to fit the above experimental data. These two kinetic equations are displayed as follows [28]:

$$\lg(q_e - q_t) = \lg q_e - \frac{k_1}{2.303}t \quad \text{pseudo-first order} \tag{1}$$

$$\frac{t}{q_t} = \frac{1}{k_2 q_e{}^2} + \frac{1}{q_e} \quad \text{pseudo-second order kinetic} \tag{2}$$

where q_e and q_t are the adsorption capacity of Hg^0 on the sorbents at equilibrium, and at reaction time t (min), respectively. The parameters k_1 (min^{-1}) and k_2 (g/(μg·min)) are the rate constants of the pseudo-first order, and pseudo-second order models, respectively.

The fitting results are shown in Figure 8, and the obtained values of correlation coefficient (R^2) are summarized in Table 2. The values of R^2 of the pseudo-second order model for αMnO_2-NR and αMnO_2-NR@TiO_2 are 0.991, and 0.995, respectively, which are higher than those of pseudo-first order kinetic model (0.944 and 0.938 for αMnO_2-NR and αMnO_2-NR@TiO_2). It indicates that the pseudo-second order model can better fit the experimental data and Hg^0 removal process are dominantly controlled by chemisorption. After SO_2 introduction, the values of R^2 of the pseudo-second order model for αMnO_2-NR and αMnO_2-NR@TiO_2 are 0.997 and 0.992, which are still much higher than those of the pseudo-first order model. These results show that Hg^0 adsorption process in the presence of SO_2 atmosphere are also dominantly controlled by chemisorption.

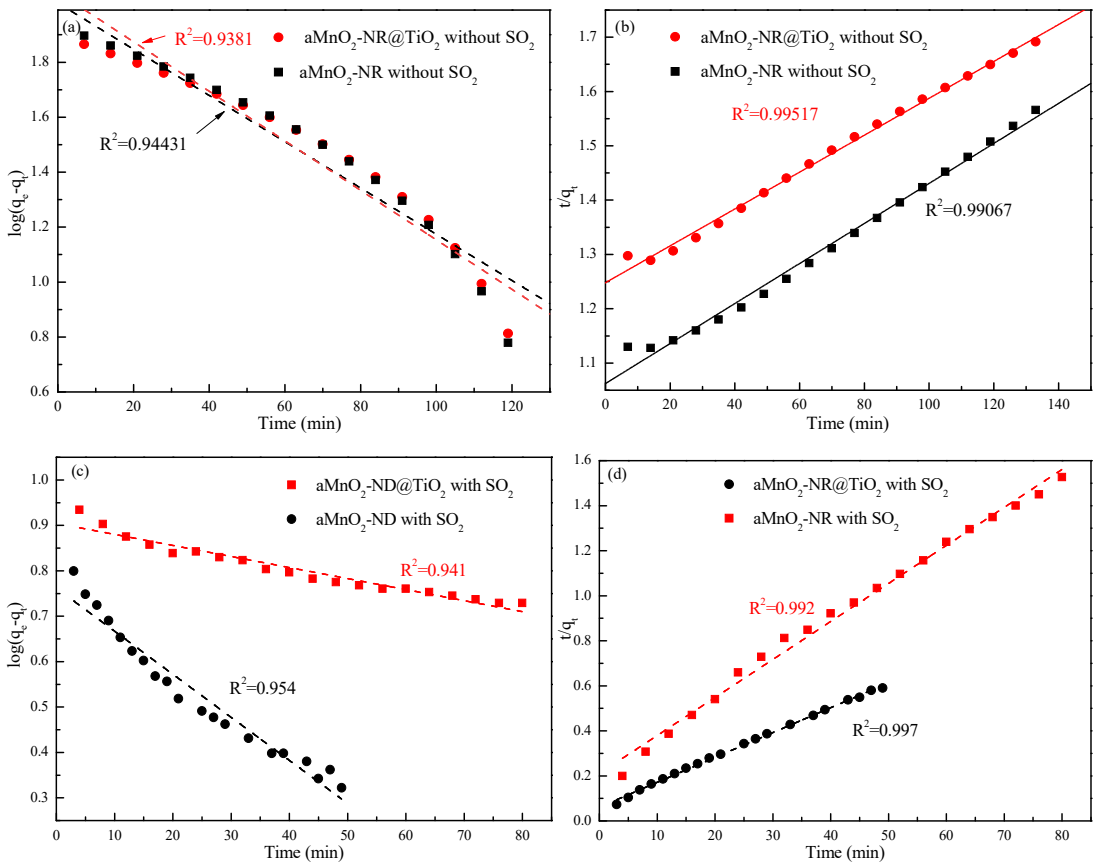

Figure 8. Kinetic analysis of Hg^0 adsorption on αMnO_2-NR and αMnO_2-NR@TiO_2 (**a**) pseudo-first order kinetic model without SO_2, (**b**) pseudo-second order kinetic model without SO_2, (**c**) pseudo-first order kinetic model with SO_2, (**d**) pseudo-second order kinetic model with SO_2.

Table 2. Kinetic parameters (R^2) of pseudo-first order and pseudo-second order models.

Kinetic Models	αMnO_2-NR without SO_2	αMnO_2-NR@TiO_2 without SO_2	αMnO_2-NR with SO_2	αMnO_2-NR@TiO_2 with SO_2
Pseudo-first (R^2)	0.944	0.938	0.954	0.941
Pseudo-second (R^2)	0.991	0.995	0.997	0.992

2.4. The Mechanism of SO_2 Effects on Hg^0 Adsorption

XPS analysis was employed to explore the relative proportion of elements on the sample surface. The XPS spectra of Mn 2p, O 1s and S 2p for the fresh and used samples are shown in Figure 9. The surface atomic concentrations and surface atomic ratios are summarized in Table 3.

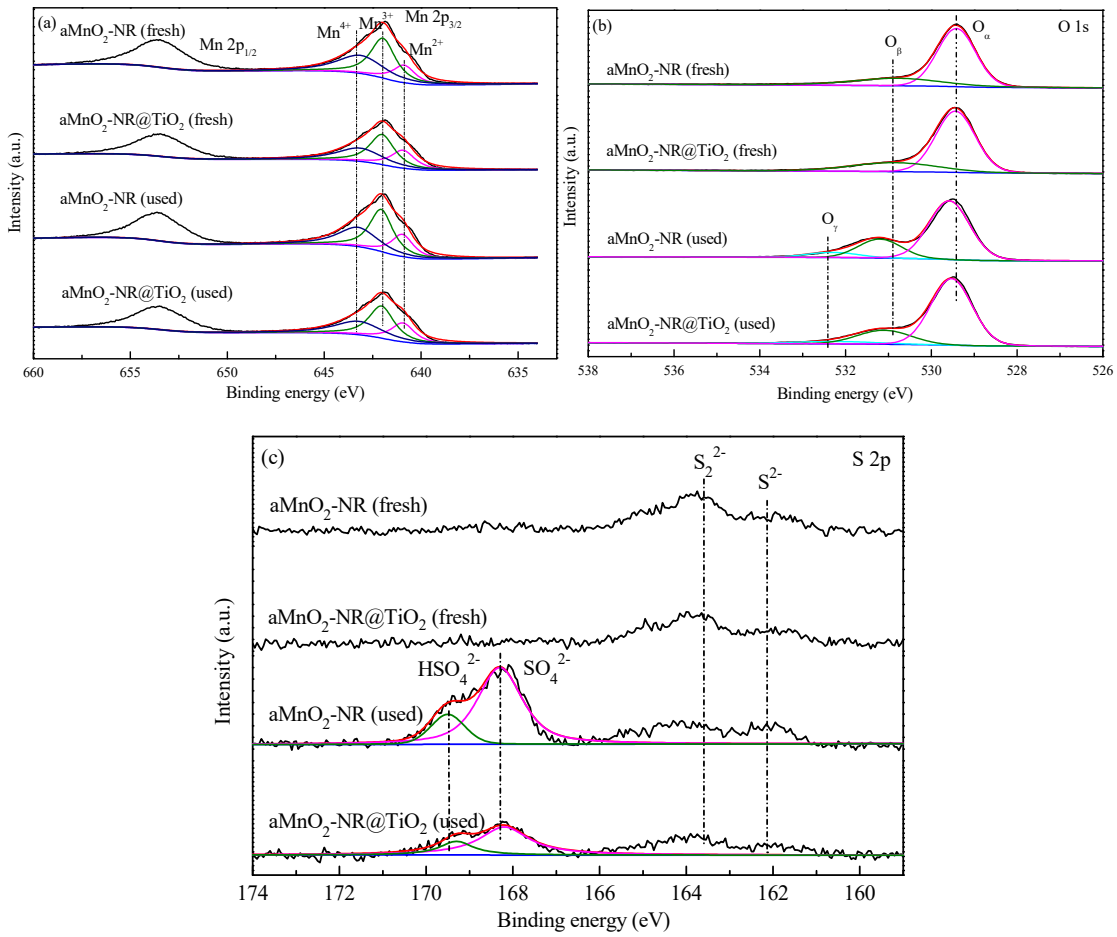

Figure 9. XPS spectra of (**a**) Mn 2p, (**b**) O 1s and (**c**) S 2p.

Table 3. The surface atomic concentrations and the relative concentration ratios of samples based on XPS.

Samples	S	Mn^{4+}/Mn	O_β/O
αMnO_2-NR (fresh)	3.17	37.8	26.0
αMnO_2-NR@TiO_2 (fresh)	2.27	33.4	24.7
αMnO_2-NR (used)	4.97	34.0	22.8
αMnO_2-NR@TiO_2 (used)	2.66	33.0	20.0

Figure 9a shows the XPS spectra of Mn 2p. A doublet due to spin orbital coupling can be detected which corresponds to Mn $2p_{3/2}$ (around 641.24 eV) and Mn $2p_{1/2}$ (around 652.82 eV). Due to the high intensity of Mn $2p_{3/2}$, it was fitted to give detail information of valence state of Mn and it can be separated into three peaks at 640.2–641.2 eV, 641.2–642.1 eV, and 642.2–643.4 eV corresponding to Mn^{2+}, Mn^{3+}, and Mn^{4+}, respectively [29,30]. As shown in Table 3, the ratio of Mn^{4+}/Mn is about 37.8% for the fresh αMnO_2-NR and it decreases to 33.4% after the SO_2 resistance test. Compared to αMnO_2-NR, Mn^{4+} content is almost constant for αMnO_2-NR@TiO_2 before, and after, SO_2 resistance test. These results indicate that, for αMnO_2-NR, Mn^{4+} is easily reduced to Mn^{2+} during SO_2 resistance process via the reaction between SO_2 and MnO_2 [31]. For αMnO_2-NR@TiO_2, the interaction between SO_2 and MnO_2 is inhibited by the TiO_2 shell structure, which can efficiently protect active component Mn^{4+} in the core.

Figure 9b shows O 1s XPS spectra. For the fresh catalysts, O 1s bands can be split into two peaks, corresponding to lattice oxygen (peak at 529.5 eV, denoted as O_α) and chemisorbed oxygen (peak at 530.8 eV, denoted as O_β), respectively [32]. Whereas, a new peak appears around 532.3 eV after SO_2

treatment, which corresponds to SO_4^{2-} (denoted as O_γ) [33]. The intensity of the peak around 532.3 eV for αMnO_2-NR@TiO_2 is weaker than that for αMnO_2-NR suggesting a lower amount of SO_4^{2-} on the used αMnO_2-NR@TiO_2 surface. Furthermore, the peaks of O_α and O_β in αMnO_2-NR have an obvious slight shift to higher binding energy after SO_2 treatment. It might be due to the formation of sulfate salts during the sulfating process [34].

To determine the above deduction, S 2p bands was further investigated and the results are shown in Figure 9c. For the fresh αMnO_2-NR and αMnO_2-NR@TiO_2, two peaks around 162.2 eV and 163.2 eV attributed to S^{2-} and S_2^{2-} can be detected [35,36], which may come from $MnSO_4$ (the precursor of MnO_2). But for the used αMnO_2-NR and αMnO_2-NR@TiO_2, two new peaks at about 168.8 eV and 170.0 eV are observed, which may be assigned to SO_4^{2-}, and HSO_4^-, respectively [37,38]. The peak intensity of the used αMnO_2-NR is much higher than that of αMnO_2-NR@TiO_2. As shown in Table 3, for αMnO_2-NR, the surface atomic concentrations of S increases from 3.17% to 4.97% after SO_2 teatment while it increases from 2.27% to 2.66% for αMnO_2-NR@TiO_2. These results confirm that TiO_2 shell can inhibit the S accumulation on catalyst surface.

To obtain more information about the SO_2 poisoning mechanism, Thermo-gravimetric-differential thermos-gravimetry (TG-DTG) was performed to investigate the weight loss of αMnO_2-NR and αMnO_2-NR@TiO_2 after SO_2 treatment, and the results are presented in Figure 10. It can be seen that the used αMnO_2-NR has an obvious weight loss step in the temperature range of 680−780 °C with a weight loss of about 2.4%, which can be attributed to manganese sulfate decomposition [39–41]. There is no weight loss step between 680−780 °C with respect to αMnO_2-NR@TiO_2, but there is a new weak step around 780–850 °C can be detected, and it may be due to the decomposition of $Ti(SO_4)O$ [42]. This result demonstrates that SO_2 tends to react with titanium oxides instead of manganese oxides over αMnO_2-NR@TiO_2. Based on these results, TiO_2 shell can lead to the preferential adsorption of SO_2 on Ti surrounding forming $Ti(SO_4)O$ to protect Mn active component from being deactivated.

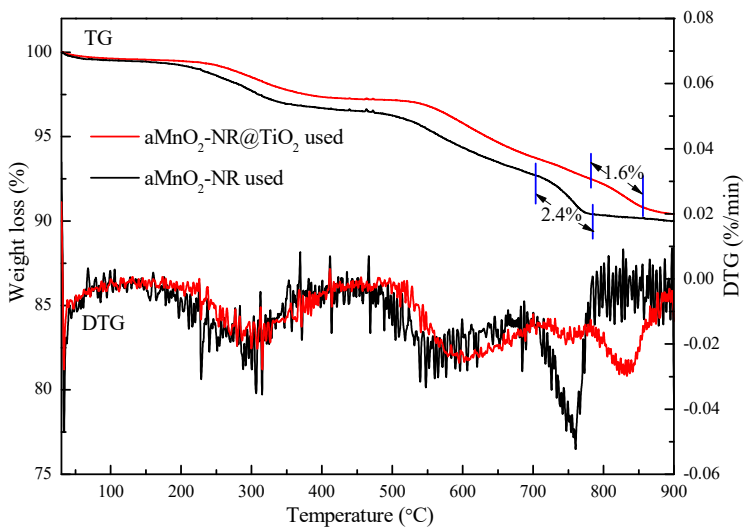

Figure 10. Thermo-gravimetric (TG) and differential thermos-gravimetry (DTG) of spectras of αMnO_2-NR and αMnO_2-NR@TiO_2 after SO_2 treatment.

3. Materials and Methods

3.1. Catalysts Preparation

The αMnO_2 nanorods were synthesized through a hydrothermal method [43]. $KMnO_4$ (2.5 g, AR) and $MnSO_4{\cdot}H_2O$ (1.05 g, AR) were dissolved in 80 mL distilled water. The mixed solution was transferred into a Teflon-line stainless steel autoclave, sealed, and kept in an oven at 160 °C for 12 h. After cooling to room temperature, the precipitates were filtered off, washed several times using

deionized water and dried at 110 °C overnight. Finally, the product was calcined at 400 °C in a muffle furnace for 4 h and the obtained sample is denoted as αMnO_2-NR.

MnO_2@TiO_2 core-shell nanorods were synthesized through a versatile kinetics-controlled coating method [44]. αMnO_2-NR (0.075 g) and aqueous ammonia (0.28 mL, 28 wt.%) were dispersed in 100 mL absolute ethanol under ultrasound for 30 min. Afterwards, titanium tetrabutoxide (TBOT) (0.75 mL) was added drop-wise into the mixture and then kept at 45 °C for 24 h. The mixed solution was filtered, washed and dried at 60 °C for 12 h. Finally, the solid was calcined under flow air at 500 °C for 2 h to obtain the sample (denoted as αMnO_2-NR@TiO_2).

ALL reagents are from Aladdin company, Shanghai, China.

3.2. Hg^0 Adsorption Experiments

The Hg^0 removal test has been described in detail in our previous work [45]. The experimental reactor contains a gas distribution system, a Hg^0 vapor generating device, a fixed-bed quartz reactor (ID = 8 mm), an online mercury analyzer and a tail gas treating unit. The mercury permeation tube was placed in a U-shape glass tube, which was immersed in a water bath at a constant-temperature (38 °C) to ensure a constant Hg^0 permeation rate. The total gas flow was 600 mL/min, and the sorbent volume was generally 0.2 mL, resulting in a GHSV of 1.8×10^5 h^{-1}. The concentrations of Hg^0 and SO_2 were monitored by a VM-3000 online mercury analyzer (Mercury Instruments, München, German), and flue gas analyzer (KM950, Kane International Ltd., London, United Kingdom), respectively.

During each test, the Hg^0 gas first bypassed the fixed-bed reactor, and then introduced into the reactor for 2 h to obtain a stable Hg^0 concentration. Hg^0 breakthrough ratio was quantified by the following formula,

$$Breakthrough\ ratio(\%) = \frac{C}{C_0} \times 100\% \quad (3)$$

where C and C_0 represent the inlet and outlet Hg^0 concentrations (μg/Nm^3) in the fixed-bed reactor.

3.3. Characterization

The morphology and microstructure of the samples were observed using SEM (Nova NanoSEM 450, FEI) and TEM (Tecnai G2 F30 S-Twin, FEI). The surface areas and pore parameters of the samples were determined by Nitrogen adsorption/desorption method at liquid nitrogen temperature at −196 °C on an automated gas sorption analyzer (Autosorb-iQ-C, Quantachrome Instruments, Boynton Beach, FL, USA). The pore size and pore volume were derived from the desorption branches using the Barrette-Joynere-Halenda (BJH) model. The crystal structures of the samples were characterized by an XRD (XRD-7000S, SHIMADZU Corporation, Kyoto, Japan) operating at 40 kV and 100 mA using a Cu Kα radiation. The scanning range (2θ) was from 10° to 90° with a scan speed of 5°/min. The element (Mn, O, and Hg) valence state was analyzed by XPS (ESCALAB250 Thermo Fisher Scientific, Wilmington, DE, USA) with a monochromatic Al Kα source. The C 1s binding energy value of 284.8 eV was used to calibrate the observed spectra. TG was performed on TGA/DSC1 analyser (METTLER TOLEDO, Schwerzenbach, Switzerland), under a nitrogen flow of 20 mL/min, using a heating rate of 10 °C/min from room temperature to 900 °C (NETZSCH Corporation, Selb, Germany). DTG analysis was obtained based on residual weight of the sample with respect to time. FTIR spectra were obtained on a Nicolet Magana-IR 750 spectrometer to measure the surface groups of the samples (Thermo Nicolet Corporation, Madison, WI, USA).

4. Conclusions

αMnO_2-NR@TiO_2 was prepared by versatile kinetics-controlled coating method to compare with αMnO_2-NR in the Hg^0 removal process. SEM, BET, and XRD results showed that TiO_2 shell did not change the structure of αMnO_2-NR. Therefore, the two sorbents had similar Hg^0 removal performance in N_2 atmosphere. When SO_2 was introduced, αMnO_2-NR@TiO_2 had a much better performance than

αMnO_2-NR. XPS and TG-DTG results showed that αMnO_2-NR@TiO_2 had lower surface S concentration after treatment of SO_2, and no manganese sulfate could be detected in αMnO_2-NR@TiO_2. It suggests that the TiO_2 shell can effectively protect MnO_2 from being deactivated by SO_2. Adsorption kinetic results showed that Hg^0 adsorption process over both the two sorbents obeys pseudo-second order model with, or without, SO_2.

Supplementary Materials: The following are available online at http://www.mdpi.com/2073-4344/10/1/72/s1, Figure S1: Outlet Hg^0 concentration without sorbent, Figure S2: The image of αMnO_2-NR@TiO_2 after adsorption, Figure S3: Breakthrough curve of αMnO_2-NR@TiO_2 with different Hg^0 feed concentration, Table S1: Comparison of the adsorption capacities of the sorbents.

Author Contributions: X.S. and H.Z. designed the experiments; X.H. and C.L. performed the experiments and analyzed the data; X.Z. wrote the paper; J.B., N.Z. and G.H. contributed reagents/materials/analysis tools. All authors have read and agreed to the published version of the manuscript.

Funding: This research was funded by [National Natural Science Foundation of China] grant number [51978124], [Liaoning Provincial Natural Science Foundation of China] grant number [20180510054].

Acknowledgments: We gratefully acknowledge the financial support of the National Natural Science Foundation of China (51978124), Liaoning Provincial Natural Science Foundation of China (20180510054), Shandong Provincial Natural Science Foundation PhD Programme (ZR2016EEB33), Foundation of China the Program for Changjiang Scholars (T2012049), Education Department of the Liaoning Province of China (LT2015007), the Fundamental Research Funds for the Central Universities (DUT18JC45).

Conflicts of Interest: The authors declare no conflict of interest.

References

1. Zhao, H.; Mu, X.; Yang, G.; George, M.; Cao, P.; Fanady, B.; Rong, S.; Gao, X.; Wu, T. Graphene-like MoS_2 containing adsorbents for Hg^0 capture at coal-fired power plants. *Appl. Energy* **2017**, *207*, 254–264. [CrossRef]
2. Zhang, J.; Duan, Y.; Zhou, Q.; Zhu, C.; She, M.; Ding, W. Adsorptive removal of gas-phase mercury by oxygen non-thermal plasma modified activated carbon. *Chem. Eng. J.* **2016**, *294*, 281–289. [CrossRef]
3. Zhang, B.; Zeng, X.; Xu, P.; Chen, J.; Xu, Y.; Luo, G.; Xu, M.; Yao, H. Using the Novel Method of Nonthermal Plasma To Add Cl Active Sites on Activated Carbon for Removal of Mercury from Flue Gas. *Environ. Sci. Technol.* **2016**, *50*, 11837–11843. [CrossRef] [PubMed]
4. Zhou, Q.; Duan, Y.F.; Hong, Y.G.; Zhu, C.; She, M.; Zhang, J.; Wei, H.Q. Experimental and kinetic studies of gas-phase mercury adsorption by raw and bromine modified activated carbon. *Fuel Process. Technol.* **2015**, *134*, 325–332. [CrossRef]
5. Liu, W.; Vidic, R.D.; Brown, T.D. Impact of Flue Gas Conditions on Mercury Uptake by Sulfur-Impregnated Activated Carbon. *Environ. Sci. Technol.* **2000**, *34*, 154–159. [CrossRef]
6. Bisson, T.M.; Xu, Z. Potential Hazards of Brominated Carbon Sorbents for Mercury Emission Control. *Environ. Sci. Technol.* **2015**, *49*, 2496–2502. [CrossRef]
7. Chen, C.; Jia, W.; Liu, S.; Cao, Y. The enhancement of CuO modified V_2O_5-WO_3/TiO_2 based SCR catalyst for Hg^0 oxidation in simulated flue gas. *Appl. Surf. Sci.* **2018**, *436*, 1022–1029. [CrossRef]
8. Li, H.; Zhang, W.; Wang, J.; Yang, Z.; Li, L.; Shih, K. Coexistence of enhanced Hg^0 oxidation and induced Hg^{2+} reduction on CuO/TiO_2 catalyst in the presence of NO and NH_3. *Chem. Eng. J.* **2017**, *330*, 1248–1254. [CrossRef]
9. Liu, T.; Xue, L.; Guo, X.; Liu, J.; Huang, Y.; Zheng, C. Mechanisms of Elemental Mercury Transformation on α-Fe_2O_3(001) Surface from Experimental and Theoretical Study: Influences of HCl, O_2, and SO_2. *Environ. Sci. Technol.* **2016**, *50*, 13585–13591. [CrossRef]
10. Zarei, S.; Niad, M.; Raanaei, H. The removal of mercury ion pollution by using Fe_3O_4-nanocellulose: Synthesis, characterizations and DFT studies. *J. Hazard. Mater.* **2018**, *344*, 258–273. [CrossRef]
11. He, C.; Shen, B.; Chi, G.; Li, F. Elemental mercury removal by CeO_2/TiO_2-PILCs under simulated coal-fired flue gas. *Chem. Eng. J.* **2016**, *300*, 1–8. [CrossRef]
12. Zhu, Y.; Han, X.; Huang, Z.; Hou, Y.; Guo, Y.; Wu, M. Superior activity of CeO_2 modified V_2O_5/AC catalyst for mercury removal at low temperature. *Chem. Eng. J.* **2018**, *337*, 741–749. [CrossRef]

13. Xu, H.; Jia, J.; Guo, Y.; Qu, Z.; Liao, Y.; Xie, J.; Shangguan, W.; Yan, N. Design of 3D MnO_2/Carbon sphere composite for the catalytic oxidation and adsorption of elemental mercury. *J. Hazard. Mater.* **2018**, *342*, 69–76. [CrossRef] [PubMed]
14. Cimino, S.; Scala, F. Removal of Elemental Mercury by MnO_x Catalysts Supported on TiO_2 or Al_2O_3. *Ind. Eng. Chem. Res.* **2016**, *55*, 5133–5138. [CrossRef]
15. Zhang, S.; Zhao, Y.; Yang, J.; Zhang, J.; Zheng, C. Fe-modified MnO_x/TiO_2 as the SCR catalyst for simultaneous removal of NO and mercury from coal combustion flue gas. *Chem. Eng. J.* **2018**, *348*, 618–629. [CrossRef]
16. Yao, T.; Duan, Y.; Zhu, C.; Zhou, Q.; Xu, J.; Liu, M.; Wei, H. Investigation of mercury adsorption and cyclic mercury retention over MnO_x/γ-Al_2O_3 sorbent. *Chemosphere* **2018**, *202*, 358–365. [CrossRef]
17. Xie, J.K.; Qu, Z.; Yan, N.Q.; Yang, S.J.; Chen, W.M.; Hu, L.G.; Huang, W.J.; Liu, P. Novel regenerable sorbent based on Zr–Mn binary metal oxides for flue gas mercury retention and recovery. *J. Hazard. Mater.* **2013**, *261*, 206–213. [CrossRef]
18. Li, H.; Wang, Y.; Wang, S.; Wang, X.; Hu, J. Removal of elemental mercury in flue gas at lower temperatures over Mn-Ce based materials prepared by co-precipitation. *Fuel* **2017**, *208*, 576–586. [CrossRef]
19. Yi, Y.; Li, C.; Zhao, L.; Du, X.; Gao, L.; Chen, J.; Zhai, Y.; Zeng, G. The synthetic evaluation of CuO-MnO_x-modified pinecone biochar for simultaneous removal formaldehyde and elemental mercury from simulated flue gas. *Environ. Sci. Pollut. Res.* **2017**, *25*, 4761–4775. [CrossRef]
20. Xu, H.; Qu, Z.; Zhao, S.; Mei, J.; Quan, F.; Yan, N. Different crystal-forms of one-dimensional MnO_2 nanomaterials for the catalytic oxidation and adsorption of elemental mercury. *J. Hazard. Mater.* **2015**, *299*, 86–93. [CrossRef]
21. Chalkidis, A.; Jampaiah, D.; Hartley, P.G.; Sabri, Y.M.; Bhargava, S.K. Regenerable α-MnO_2 nanotubes for elemental mercury removal from natural gas. *Fuel Process. Technol.* **2019**, *193*, 317–327. [CrossRef]
22. Zhang, X.; Li, Z.; Wang, J.; Tan, B.; Cui, Y.; He, G. Reaction mechanism for the influence of SO_2 on Hg^0 adsorption and oxidation with $Ce_{0.1}$-Zr-MnO_2. *Fuel* **2017**, *203*, 308–315. [CrossRef]
23. Yang, Z.; Li, H.; Liu, X.; Li, P.; Yang, J.; Lee, P.H.; Shih, K. Promotional effect of CuO loading on the catalytic activity and SO_2 resistance of MnO_x/TiO_2 catalyst for simultaneous NO reduction and Hg^0 oxidation. *Fuel* **2018**, *227*, 79–88. [CrossRef]
24. Li, H.; Wu, C.Y.; Li, Y.; Zhang, J. Superior activity of MnO_x-CeO_2/TiO_2 catalyst for catalytic oxidation of elemental mercury at low flue gas temperatures. *Appl. Catal. B* **2012**, *111*, 381–388. [CrossRef]
25. Mitsudome, T.; Yamamoto, M.; Maeno, Z.; Mizugaki, T.; Jitsukawa, K.; Kaneda, K. One-step Synthesis of Core-Gold/Shell-Ceria Nanomaterial and Its Catalysis for Highly Selective Semihydrogenation of Alkynes. *J. Am. Chem. Soc.* **2015**, *137*, 13452–13455. [CrossRef] [PubMed]
26. Wu, J.; Zhou, T.; Wang, Q.; Umar, A. Morphology and chemical composition dependent synthesis and electrochemical properties of MnO_2-based nanostructures for efficient hydrazine detection. *Sens. Actuators B* **2016**, *224*, 878–884. [CrossRef]
27. Tabish, T.A.; Memon, F.A.; Gomez, D.E.; Horsell, D.W.; Zhang, S. A facile synthesis of porous graphene for efficient water and wastewater treatment. *Sci. Rep.* **2018**, *8*, 1817. [CrossRef]
28. McKay, G.; Ho, Y.S. Pseudo-second order model for sorption processes. *Process Biochem.* **1999**, *34*, 451–465.
29. Zhang, D.; Hou, L.A.; Chen, G.; Zhang, A.; Wang, F.; Wang, R.; Li, C. Cr Doping MnO_x Adsorbent Significantly Improving Hg^0 Removal and SO_2 Resistance from Coal-Fired Flue Gas and the Mechanism Investigation. *Ind. Eng. Chem. Res.* **2018**, *57*, 17245–17258. [CrossRef]
30. Hu, H.; Cai, S.; Li, H.; Huang, L.; Shi, L.; Zhang, D. Mechanistic Aspects of deNO_x Processing over TiO_2 Supported Co–Mn Oxide Catalysts: Structure–Activity Relationships and In Situ DRIFTs Analysis. *ACS Catal.* **2015**, *5*, 6069–6077. [CrossRef]
31. Xu, H.; Qu, Z.; Zong, C.; Quan, F.; Mei, J.; Yan, N. Catalytic oxidation and adsorption of Hg0 over low-temperature NH_3-SCR $LaMnO_3$ perovskite oxide from flue gas. *Appl. Catal. B* **2016**, *186*, 30–40. [CrossRef]
32. Peng, Y.; Qu, R.; Zhang, X.; Li, J. The relationship between structure and activity of MoO_3-CeO_2 catalysts for NO removal: Influences of acidity and reducibility. *Chem. Commun.* **2013**, *49*, 6215–6217. [CrossRef] [PubMed]
33. Ma, Y.; Mu, B.; Zhang, X.; Yuan, D.; Ma, C.; Xu, H.; Qu, Z.; Fang, S. Graphene enhanced Mn-Ce binary metal oxides for catalytic oxidation and adsorption of elemental mercury from coal-fired flue gas. *Chem. Eng. J.* **2019**, *358*, 1499–1506. [CrossRef]

34. Reddy, B.M.; Sreekanth, P.M.; Yamada, Y.; Xu, Q.; Kobayashi, T. Surface characterization of sulfate, molybdate, and tungstate promoted TiO_2-ZrO_2 solid acid catalysts by XPS and other techniques. *Appl. Catal. A* **2002**, *228*, 269–278. [CrossRef]
35. Li, H.; Zhu, L.; Wang, J.; Li, L.; Shih, K. Development of Nano-Sulfide Sorbent for Efficient Removal of Elemental Mercury from Coal Combustion Fuel Gas. *Environ. Sci. Technol.* **2016**, *50*, 9551–9557. [CrossRef] [PubMed]
36. Liao, Y.; Chen, D.; Zou, S.; Xiong, S.; Xiao, X.; Dang, H.; Chen, T.; Yang, S. Recyclable Naturally Derived Magnetic Pyrrhotite for Elemental Mercury Recovery from Flue Gas. *Environ. Sci. Technol.* **2016**, *50*, 10562–10569. [CrossRef]
37. Yang, S.; Guo, Y.; Yan, N.; Wu, D.; He, H.; Xie, J.; Qu, Z.; Jia, J. Remarkable effect of the incorporation of titanium on the catalytic activity and SO_2 poisoning resistance of magnetic Mn–Fe spinel for elemental mercury capture. *Appl. Catal. B Environ.* **2011**, *101*, 698–708. [CrossRef]
38. Xu, W.; He, H.; Yu, Y. Deactivation of a Ce/TiO_2 Catalyst by SO_2 in the Selective Catalytic Reduction of NO by NH_3. *J. Phys. Chem. C* **2009**, *113*, 4426–4432. [CrossRef]
39. Yu, J.; Guo, F.; Wang, Y.; Zhu, J.; Liu, Y.; Su, F.; Gao, S.; Xu, G. Sulfur poisoning resistant mesoporous Mn-base catalyst for low-temperature SCR of NO with NH_3. *Appl. Catal. B Environ.* **2010**, *95*, 160–168. [CrossRef]
40. Zhang, A.; Zhang, Z.; Lu, H.; Liu, Z.; Xiang, J.; Zhou, C.; Xing, W.; Sun, L. Effect of Promotion with Ru Addition on the Activity and SO_2 Resistance of MnO_x–TiO_2 Adsorbent for Hg^0 Removal. *Ind. Eng. Chem. Res.* **2015**, *54*, 2930–2939. [CrossRef]
41. Wu, Z.; Jin, R.; Wang, H.; Liu, Y. Effect of ceria doping on SO_2 resistance of Mn/TiO_2 for selective catalytic reduction of NO with NH_3 at low temperature. *Catal. Commun.* **2009**, *10*, 935–939. [CrossRef]
42. Gardy, J.; Hassanpour, A.; Lai, X.; Ahmed, M.H. Synthesis of Ti(SO_4)O solid acid nano-catalyst and its application for biodiesel production from used cooking oil. *Appl. Catal. A* **2016**, *527*, 81–95. [CrossRef]
43. Liang, S.; Teng, F.; Bulgan, G.; Zong, R.; Zhu, Y. Effect of phase structure of MnO_2 nanorod catalyst on the activity for CO oxidation. *J. Phys. Chem. C* **2008**, *112*, 5307–5315. [CrossRef]
44. Li, W.; Yang, J.; Wu, Z.; Wang, J.; Li, B.; Feng, S.; Deng, Y.; Zhang, F.; Zhao, D. A versatile kinetics-controlled coating method to construct uniform porous TiO_2 shells for multifunctional core–shell structures. *J. Am. Chem. Soc.* **2012**, *134*, 11864–11867. [CrossRef]
45. Zhang, X.; Cui, Y.; Wang, J.; Tan, B.; Li, C.; Zhang, H.; He, G. Simultaneous removal of Hg^0 and NO from flue gas by $Co_{0.3}$-$Ce_{0.35}$-$Zr_{0.35}O_2$ impregnated with MnO_x. *Chem. Eng. J.* **2017**, *326*, 1210–1222. [CrossRef]